RSC Advances

ROYAL SOCIETY OF CHEMISTRY

www.rsc.org/advances

RSC Advances

RSC Publishing

COMMUNICATION

TiO_2-pillared Clays with Well-ordered Porous Structure and Excellent their Photocatalytic Activity

Cite this: DOI: 10.1039/x0xx00000x

Jae-Hun Yang,[a] Huiyan Piao,[a] Ajayan Vinu,[b] Ahmed A. Elzatahry,[c] Seung-Min Paek[d] and Jin-Ho Choy*[a,b]

Received 00th January 2012,
Accepted 00th January 2012

DOI: 10.1039/x0xx00000x

www.rsc.org/

TiO_2-pillared clays with well-ordered porous structure are successfully prepared via incorporating TiO_2 nano-sol particles into the clays, where empty octahedral sites are partially modified with divalent metal ions such as Mg^{2+} and Fe^{2+}. The prepared TiO_2-pillared mica exhibits excellent photocatalytic activity which can be controlled by tuning the optical transparency of clay support rather than the specific surface area of the hybrid catalysts.

Layered silicates including cationic clays have been widely employed as adsorbents,[1-2] fillers,[3] catalysts,[4-5] catalyst supports,[6-7] drug delivery carriers,[8] etc. To introduce better physicochemical functions on the layered silicates, organic or inorganic functional molecules were incorporated into the interlayer space via intercalation and/or grafting reaction. In the last decades, however, many studies have been focused on nanoporous clays, namely pillared clays, whose pore sizes are larger than those of the typical zeolites. However, most of the pillared clays appeared in the literatures so far have been prepared by intercalating nanosized metal oxides such as SiO_2, TiO_2, Al_2O_3, ZrO_2, SiO_2-TiO_2, SiO_2-CoO, SiO_2-Fe_2O_3, SiO_2-Cr_2O_3, etc, into the clay layers followed by the calcination process.[8-16] In such a way, pillared clays have been eventually realized with a large specific surface area, a high thermal stability and enhanced catalytic activity.

Among various pillared clays, TiO_2- and Fe_2O_3-pillared clays have been applied to the photocatalytic reactions involving photodecomposition of environmental contaminants such as organic dyes, halogenated hydrocarbons, pesticides, and the photolysis of water.[7,13-14] The TiO_2- and Fe_2O_3-pillared clays exhibit interesting two-dimensional (2D) clay lattice which makes them unique for photocatalysis because the photocatalytic property of semiconductors[15] such as bulk titania or ferric oxide is mainly dictated by their electronic structure (band gap energy), particles size, and specific surface area. As the 2D clay lattice structure can help to avoid the agglomeration of the nanoparticles, the pillared clays with high specific surface area and porosity, and enhanced catalytic property can be easily realized.

In the heterogeneous catalysis, well-ordered pillared structure with regular pore size such as Al_2O_3-pillared clay is considered as a quite attractive catalyst due to size and shape selective catalytic reaction similar to that of zeolite catalyst. However, the reports on the preparation of well-ordered porous TiO_2-pillared clays are quite limited[10] even though many studies have reported the TiO_2-pillared clays.[13] In pillaring TiO_2 nanoparticles into the clay layers, the layer charge density of clay support as well as the regular size of positively charged TiO_2 nanoparticles is an important factor as it controls the intercalation of guest into the clay layers. In this study, we intend to demonstrate synthetic route to well-ordered TiO_2-pillared clays with different transparency and porosity by controlling the layer charge density of host clay, and finally to correlate them with photocatalytic activities.

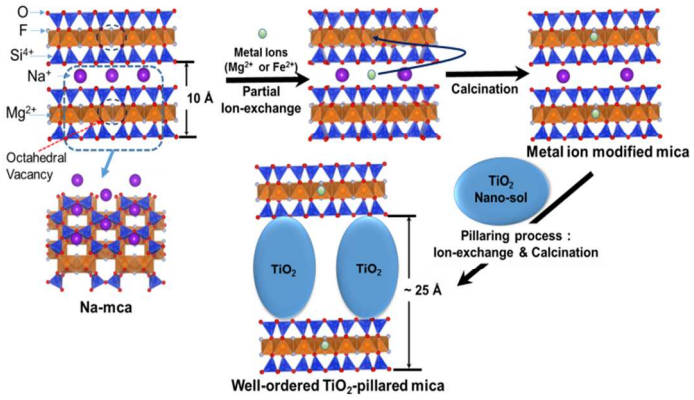

Scheme 1. Synthesis of well-ordered TiO_2-pillared clay.

The layer charge density of optically transparent Na-mica could be modified by partially incorporating Mg^{2+} or Fe^{2+} ions into the vacant octahedral Mg^{2+} defect sites through the ion-exchange

reaction (Scheme 1), and the subsequent calcination (hereafter denoted as MgM and FeM, respectively). The cation exchange capacity (CEC) of Na-mica (100 meq/g) was decreased to 75 and 67 meq/g for MgM and FeM, respectively, due to the decrease in layer charge density caused by the fixation of Mg^{2+} or Fe^{2+} ions in vacant octahedral defect sites (Hofmann-Klemen effect) (Scheme 1 and Fig. S1, ESI†).[16]

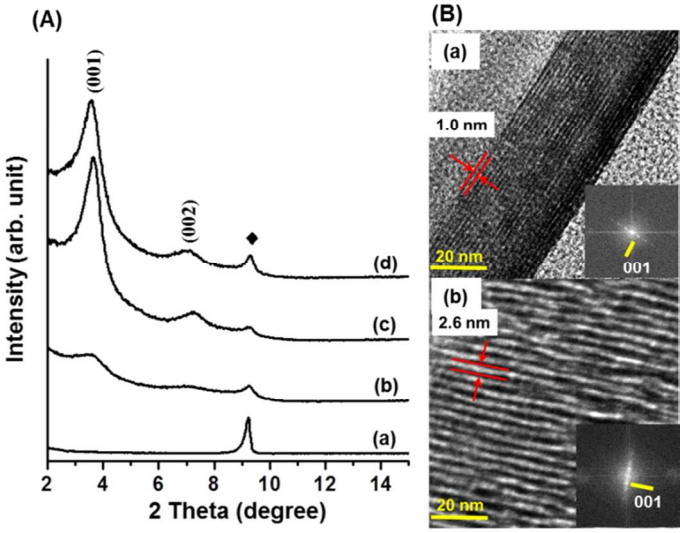

Fig. 1 (A) XRD patterns of (a) Na-mica, (b) TM-500, (c) TMgM-500 and (d) TFeM-500 (♦ corresponds to non-swellable mica), and (B) TEM images and their corresponding FFT diffractograms (insets) of the cross-sectioned (a) MgM and (b) TMgM-500.

Nanoporous TiO_2-pillared clays could be prepared by incorporating TiO_2 nanoparticles into the metal-ion modified mica (MgM and FeM) via the ion-exchange reaction and subsequent calcination. The resulting TiO_2-pillared mica, MgM and FeM calcined at 500 °C are denoted as TM-500, TMgM-500 and TFeM-500, respectively. According to the XRD patterns of TiO_2-pillared clays as shown in Figure 1 (A), the basal spacings increased to 24.5 Å, 24.3 Å and 24.7 Å for TM-500, TMgM-500 and TFeM-500, respectively, compared to that of the pristine Na-mica (9.6 Å), MgM and FeM. Such a large basal expansion along the c-axis provides a good evidence of the intercalation of TiO_2 nanoparticles into clay layers to form porous TiO_2-pillared clays. The size of the pores was estimated to be ~15 Å which was obtained by subtracting the basal spacing of the pristine (~9.6 Å) from those of the TiO_2-pillared clays. Moreover, no impurity peaks, corresponding to the anatase-, rutile- or brookite-structure of TiO_2 were observed (Fig. S2, ESI†). For TMgM-500 and TFeM-500, well-developed *(00l)* diffraction peaks (at least second order) are appeared which are ascribed to the regular stacking of TiO_2 nanoparticles in-between the silicate layers. These results indicate that the lower layer charge density of the pristine is critical to obtain the TiO_2-pillared clay with a better crystallity. As can be seen in Fig. 1(B), the periodically ordered layered structure along the crystallographic c-axis was reconfirmed by the cross-sectional TEM images and Fourier filtered images of pristine clay (MgM) and TiO_2-pillared clay (TMgM-500). The basal spacings measured between the two lattice fringes for MgM(a) and TMgM-500(b) were 10 Å and 26 Å, respectively, which are in excellent agreement with those determined from XRD measurements.

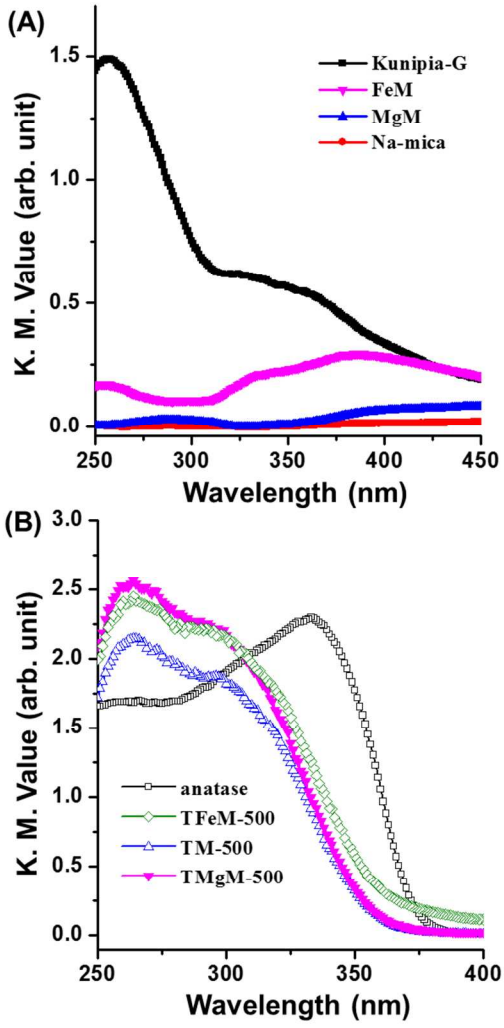

Fig. 2 Diffuse reflectance UV-vis spectra for (A) various layered silicates; Kunipia-G, Na-mica, MgM and FeM, and (B) anatase TiO_2, TM-500, TMgM-500 and TFeM-500.

The diffuse reflectance UV-vis spectra of Na-mica modified with Mg^{2+} and Fe^{2+} ions, MgM and FeM, are represented in Figure 2 (A) along with those of the pristines, Na-mica and Kunipia-G (natural montmorillonite containing Fe ions). As can be clearly seen, Na-mica and MgM can hardly absorb the light in the wavelength range of 300 nm – 350 nm due to their optical transparency, but Kunipia-G and FeM absorb the light in the same range, because the transition metal ion like Fe^{2+} is stabilized in octahedral site of clay lattice, and eventually absorb the UV and visible lights. Therefore, Na-mica and MgM could be considered as the good photocatalyst supports for immobilizing photo-active species like TiO_2 due to their good transparency in the range of UV and visible light. As shown in Fig. 2(B), the absorption edges of TM-500, TMgM-500 and TFeM-500

are blue-shifted from that of the anatase-type TiO_2 owing to the quantum size effect of TiO_2 nano-pillars stabilized in the interlayer space of 2D-clay lattice.[17] The bandgap energy calculated from the absorption edge was determined to be 3.46 eV for TM-500 and TMgM-500, and 3.38 eV for TFeM-500, respectively, which is higher than that for anatase-type TiO_2 (3.28 eV). All these results are in good agreement with the XRD analyses as the size of TiO_2 nanopillars in the 2D-clay lattice was determined to be even <2 nm. The small difference in bandgap energy among TiO_2-pillared clays is mainly due to the slight size difference (~ 1 Å) of TiO_2 pillars in the 2D-clay lattice.

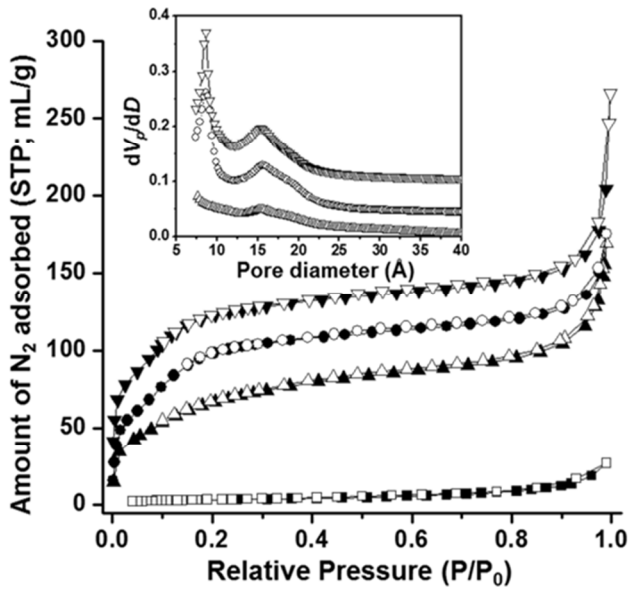

Fig. 3 N_2 adsorption-desorption isotherms of various TiO_2-pillared clays together with pristine Na-mica (square ■); TM-500 (triangle ▲), TMgM-500 (inverted triangle ▼), TFeM-500 (circle ●). Solid and open symbols indicate adsorption and desorption curves, respectively. TMgM-500, was plotted by y-axis off-set of 25. (Inset: Horváth-Kawazoe pore size distribution of TM-500, TMgM-500 and TFeM-500).

From the nitrogen adsorption-desorption isotherm analysis as shown in Fig. 3 and Table S2 (ESI†), it is clearly seen that the amount of nitrogen adsorbed at the lower relative pressure is quite negligible at 77 K. However, after TiO_2 pillaring, the amount of the nitrogen adsorbed at the lower relative pressure, which is directly related to the specific surface area of the samples is significantly improved. This is due to the fact that the incorporation of the TiO_2 nanoparticles into the silicate layers creates the nanoporosity which is responsible for the enhancement in the amount of adsorption. The isotherms of TiO_2-pillared clays, TM-500, TMgM-500 and TFeM-500, are of type I according to the Brunauer, Deming, Deming, and Teller (BDDT) classification, and free from hysteresis loop. It is interesting to note that the feature of adsorption and desorption behaviors is quite similar to that of zeolite (a typical microporous material), indicating that all the samples are microporous in nature.[18-19] This result is different from other reports, in which the isotherm curves of TiO_2 pillared clay was classified as Type IV (typical isotherm of mesoporous materials),[10,13] indicating that TiO_2 nanoparticles with homogeneous size (< 2 nm) are regularly stacked in-between the mica layers. Based on the t-plot analyses with the statistical t thickness from Harkins-Jura equation,[18-19] the micropore volume for TM-500, TMgM-500 and TFeM-500 was determined as 0.10 mL/g, 0.15 mL/g and 0.15 mL/g respectively. Each value corresponds to more than ~ 50% of each total pore volume. The Brunauer–Emmett–Teller (BET) specific surface area and total pore volume of all the TiO_2-pillared clays are in the range of 242 – 347 m^2/g and 0.21 – 0.29 mL/g, respectively. These values are much higher as compared to those of Na-mica (9 m^2/g and 0.03 mL/g), confirming the formation of nanoporosity in the samples. In particular, it is interesting to note that the specific surface area and the pore volume of TMgM-500 (335 m^2/g & 0.29 mL/g) and TFeM-500 (347 m^2/g & 0.27 mL/g) are much higher than those of TM-500 (242 m^2/g & 0.21 mL/g), which is mainly due to the formation of highly ordered TiO_2-pillar with nanoporous structure. Furthermore, the Horbáth-Kawazoe pore size distribution of all the samples shows a broad peak at ~15 Å, which is also well consistent with the gallery height of the TiO_2-pillared clays obtained from the XRD results. Moreover, a sharp peak at ~8 Å for well-ordered TiO_2 pillared clays such as TMgM-500 and TFeM-500 is observed, which is assigned to the inter-particle distance among TiO_2 nanoparticles regularly incorporated between 2D-clay lattices.

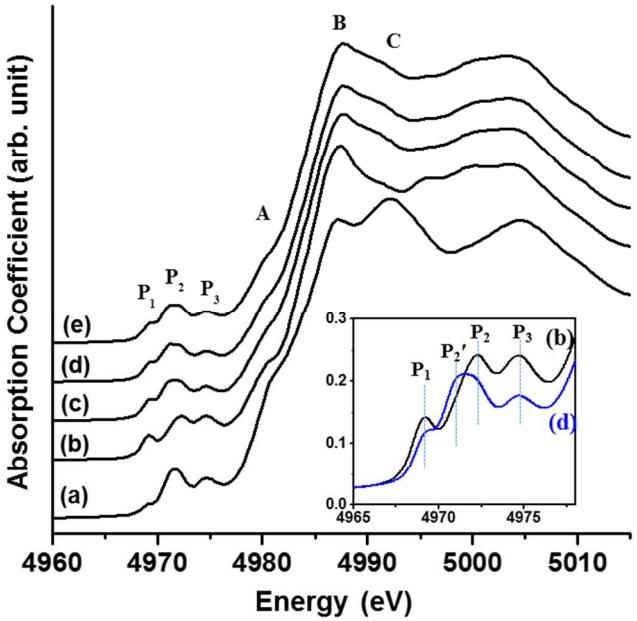

Fig. 4 Normalized Ti K-edge XANES spectra for (a) rutile-type TiO_2, (b) anatase-type TiO_2, (c) TM-500, (d) TMgM-500 and (d) TFeM-500**.**

To elucidate the local symmetry of titanium atoms in the samples, the X-ray absorption near-edge structure (XANES) analysis was also performed for all the TiO_2-pillared clays.[21] As shown in Fig. 4, the overall feature of Ti K-edge XANES spectra for TM-500, TMgM-500 and TFeM-500 was similar to that for anatase-type TiO_2 rather

than that for rutile-type one. The weak peaks (P_1, P_2 and P_3) corresponding to the dipole-forbidden transitions from 1s to 3d-4p hybrid orbital, t_{2g} and e_g, respectively, were observed for all the TiO_2-pillared samples and the reference anatase-TiO_2 and rutile-type one, indicating that titanium ions in the TiO_2 pillars were in pseudo-octahedral symmetry.[12,22-24] The data of TiO_2-pillared clays were also analyzed based on the previous study done by Farges et al.[22] on the position and intensity P_2 peak. It was found that ~ 90% of Ti^{4+} ions in the TiO_2 pillar were high in symmetry, six coordinated, but ~10% of them were stabilized in a lowered symmetric site, five coordinated site. Those coordinatively unsaturated symmetry for Ti^{4+} ions surely originated from the surface contribution of nano-sized TiO_2 pillars, where the oxygen defects are abundant. In the main edge region, three spectral features denoted as A, B and C were observed, where the lower energy peak A was related to the transition with the shakedown process whereas the higher energy peaks, B and C, were assigned as the transition from core 1s to out-of-plane $4p_z$ orbital and to in-plane $4p_{x,y}$ orbitals.[24] The peak positions and intensities for all the TiO_2-pillared clays were very similar to those for anatase-type bulk TiO_2, whereas the overall spectral feature and the peak C intensity, in particular, for rutile-type bulk TiO_2 were completely different from others, owing to the fact that the local symmetry around Ti atoms in rutile TiO_2 is tetragonally less distorted than that in anatase and TiO_2-pillared clays.

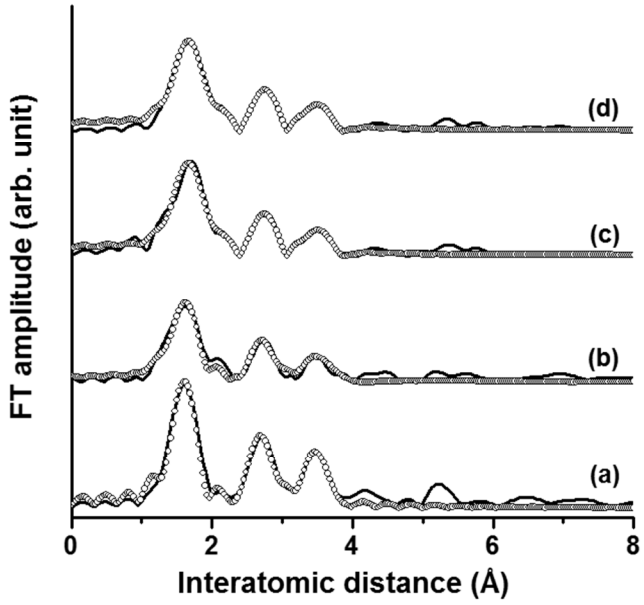

Fig. 5 k^3-weighted Ti K-edge EXAFS spectra for (a) anatase-type TiO_2, (b) TM-500, (c) TMgM-500 and (d) TFeM-500. Their best-fitted spectra (open circles) are compared with experimental spectra (solid lines). The fourier fitting range is R = 1.0 – 3.85 Å.

In addition to the XANES study, we conducted the extended X-ray absorption fine structure (EXAFS) analysis for the pillared samples, since the local structural symmetry of TiO_2 pillars is closely related to the photocatalytic activity. As shown in Fig. 5, the Fourier transforms (FTs) of the Ti K-edge k^3-weighted EXAFS spectra of the pillared clays were investigated along with that of bulk anatase TiO_2 as a reference material. In the bulk anatase, the FT peaks at 1.6, 2.7, and 3.5 Å are attributed to the contribution of (Ti-O), (Ti-Ti_{edge}), and (Ti-Ti_{corner}) bonds, respectively, and the structural parameters are listed in Table S3 (ESI†). Even though the bond distances of TiO_2 pillared clays are determined to be virtually identical to those of the bulk anatase TiO_2, the coordination numbers of the edge- and corner-shared (Ti-Ti) shells for the formers are smaller than those for the latter, which are in good agreement with the XANES results. These results indicate the structural disorder of oxygen atoms around Ti atoms due to the formation of nanosized TiO_2 pillars in the interlayer space of clays as evidenced by the XRD analysis, nitrogen adsorption measurements, and XANES results. In contrast, the FT peaks beyond 4 Å, ascribed to the multiple scattering effect from the surrounding atoms, are also reduced in the pillared clays, highlighting the damping of the EXAFS signal because of the nanosized flexible structure of TiO_2 pillars.

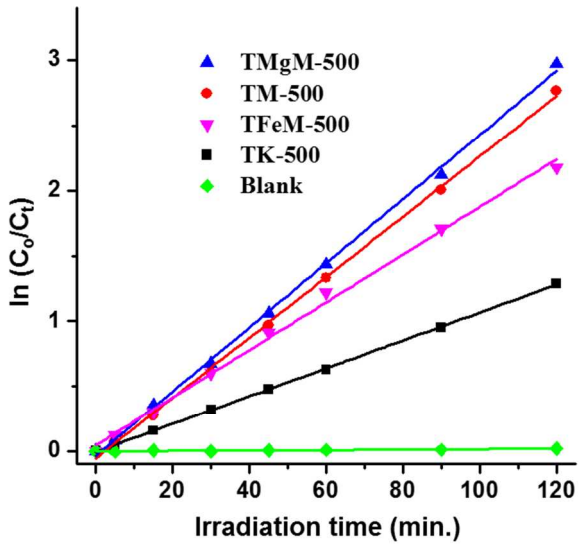

Fig. 6 Time-dependent curves of the concentration of methyl orange (MO) upon photocatalytic degradation reaction under UV irradiation ($\lambda > 290$ nm, 0.1 W/cm^2) with and without TiO_2-pillared clays; TK-500, TM-500, TMgM-500, TFeM-500 and blank (without catalyst). Initial concentration of MO was 5×10^{-5} mol/L and 30 mg of catalyst was dispersed in 30 mL MO solution.

To evaluate the photocatalytic activity of the well-ordered TiO_2-pillared clays with nanoporous structure, the time-dependent concentration variation of methyl orange (MO) was measured in an aqueous solution suspended with TiO_2-pillared clays under UV irradiation ($\lambda > 290$ nm), since MO is one of the model compounds largely used for the evaluation of photodecomposition activity.[7] Fig. 6 shows the fractional concentration of MO in the TiO_2-pillared clay suspensions depending on the UV irradiation time compared to that in TiO_2-pillared Kunipia-G (denoted as TK-500), in which the photodecomposition kinetic constants were determined by fitting the curves based on the peudo-first order kinetic equation.[7,25] Under this

photocatalytic reaction condition, the concentration of MO with the TiO_2-pillared clay catalysts decreased drastically upon increasing the UV light irradiation time, whereas no photocatalytic degradation of MO was observed without photocatalyst within 120 min. The order of the photodecomposition activity is as follows; TMgM-500 > TM-500 > TFeM-500 > TK-500. In general, the catalysts with larger specific surface area show higher activity, confirming the importance of nanoposity in the catalyst. Comparing TMgM-500 and TFeM-500 with the similar specific surface area (~340 m^2/g) and TiO_2 contents (~32 wt%), the photocatalytic activity of TMgM is higher than that of TFeM-500.

It is important to note that the photocatalytic activity of TK-500 (with less transparent clay support; Kunipia-G) is found to be much lower than that of TM-500 (with transparent clay support; Na-mica) even though TK-500 has much higher TiO_2 content (56.9 wt%) and specific surface area (314 m^2/g) than those of TM-500 (34.0 wt% and 242 m^2/g). We believe that such unusual photocatalytic property of the TiO_2-pillared clays with different textural parameters is due to the difference in the optical transparency of the host clay layers. According to UV-vis spectroscopic analysis (Fig. 2(A)), the order of the absorption value (Kubelka Munk (K.M.) value) at the absorption edge (~350 nm) is Kuinipia-G (0.55) > FeM (0.23) > MgM (0.01) and Na-mica (0.00), indicating that some part of the irradiated photoenergy in the TiO_2-pillared clay is shielded in the cases of less transparent clay such as Kunipia-G and FeM. Therefore, it is quite clear why photodegradation activity of MO was higher in the presence of TiO_2-pillared in transparent clays; TMgM-500 (k = 0.025 $min.^{-1}$) > TM-500 (k = 0.023 $min.^{-1}$) > TFeM-500 (k = 0.018 $min.^{-1}$) > TK-500 (k = 0.011 $min.^{-1}$). This result is quite similar to the order of optical transparency of the pristine clay support. If the TiO_2 photocatalysts are supported on clays with similar optical transparency such as Na-mica and MgM, the photocatalytic activity of TM-500 should be equivalent to or slightly higher than that of TMgM-500. However, the specific surface area of TMgM-500 is quite higher than that of TM-500, resulting in slightly higher photocatalytic activity, because of the cancelling effect (optical transparency ⇆ specific surface area). All these results reflect that the optical transparency as well as the specific surface area of the catalyst support (clay) is an important factor that controls the photocatalytic performance of the photocatalyt immobilized clays.

Conclusions

The layer charge density and optical transparency of sodium fluoromica were modified by incorporating Mg^{2+} and Fe^{2+} cations partially into the empty octahedral sites of Na-mica by using HK effect. Heterogeneous microporous TiO_2 photocatalysts with well-ordered nanoporous structure were also successfully synthesized by intercalating TiO_2 nanoparticles into the clay layers via ion-exchange reaction and subsequent calcination. The prepared TiO_2-pillared clays were highly porous and exhibited the specific surface areas of 242 – 347 m^2/g and large pore volume of 0.21 – 0.29 mL/g which were much higher as compared to those of the pristine clay (~10 m^2/g), in which more than ~50% of total pore volume is composed of micropores. From the XANES and EXAFS analyses at the Ti K-edge, the local symmetry of Ti in TiO_2-pillared clays was fairly similar with that in anatase and was found to be slightly lower because of the formation of oxygen deficient TiO_2 nano-pillars in-between the clay sheets. The order of photocatalytic activity of TiO_2-pillared clays on photodegradation of methyl orange under UV irradiation was determined to be TMgM-500 > TM-500 > TFeM-500 > TK-500. It was found that the photocatalytic acivity of TiO_2-pillared clays is significantly affected by the optical transparency of host clay lattice as well as the specific surface area.

Acknowledgements

This work was supported by the National Research Foundation of Korea (NRF) grant, funded by the Korea government (MSIP) (2005-0049412 and 2013R1A1A2062239) and by the Ewha Womans University Research Grant of 2013. One of the authors A. V thanks Australian Research Council for the Future Fellowship.

Notes and references

[a]Center for Intelligent Nano-Bio Materials (CINBM), Department of Chemistry and Nano Science, Ewha Womans University, Seoul 120-750, Republic of Korea. *jhchoy@ewha.ac.kr.

[b]Australian Institute for Bioengineering and Nanotechnology, The University of Queensland, Brisbane 4073, QLD, Australia.

[c]Department of Chemistry, King Saud University, B.O. BOX.2455 Riaydh 11451 Saudi Arabia.

[d]Department of Chemistry and Green-Nano Materials Research Center, Kyungpook National University, Taegu 702-701, Republic of Korea.

†Electronic Supplementary Information (ESI) available: [details of any supplementary information available should be included here]. See DOI: 10.1039/c000000x/

1 M. Park, D. H. Lee, C. L. Choi, S. S. Kim, K. S. Kim and J. Choi, *Chem. Mater.*, 2002, **14**, 2582.

2 Y. Ide, N. Ochi and M. Ogawa, *Angew. Chem. Int. Ed.*, 2011, **50**, 654.

3 E. Ruiz-Hitzky, M. Darder, F. M. Fernandes, B. Wicklein, A.C.S. Alcantara and P. Aranda, *Prog. Polymer Sci.*, 2013, **38**, 1392.

4 J. M. Adams and R.W. McCabe in *Handbook of Clay Science Vol. 1* (Eds.: F. Bergaya, B.K.G. Theng and G. Lagaly), Elsevier, Netherlands, 2006, pp. 541-581.

5 A. Olaya, S. Moreno and R. Molina, *Applied Catalysis A: General*, 2009, **370**, 7–15.

6 P. Cool and E. F. Vansant in *Handbook of Layered Materials* (Eds.: S.M. Auerbach, K.A. Carrado and P. K. Dutta), Marcel Dekker Inc, New York, 2004, pp. 261-311.

7 S. Liu, J. H. Yang and J. H. Choy, *J. Photochem. Photobiol. A: Chem.*, 2006, **179**, 75.

8 (a) H. Jung, H. M. Kim, Y. B. Choy and J. H. Choy, *Int. J. Pharm.*, 2008, **349**, 283; (b) J. H. Yang, H. Jung, S. Y. Kim and J. H. Choy, *J. Nanosci. Nanotechnol.*, 2013, **13**, 7331.

9 (a) T. J. Pinnavaia, T. J. *Science*, 1983, **220**, 365; (b) K. Ohtsuka, *Chem. Mater.*, 1997, **9**, 2039.
10 (a) S. Yamanaka, T. Nishihara and M. Hattori, *Mater. Chem. Phys.*, 1987, **17**, 87; (b) S. Yamanaka and K. C. Makita, *J. Porous Mater.*, 1995, **1**, 29.
11 J. H. Park, J. H. Yang, J. B. Yoon, S. J. Hwang and J. H. Choy, *J. Phys. Chem. B*, 2006, **110**, 1592.
12 a) J. H. Choy, H. Jung, Y. S. Han, J. B. Yoon, Y. G. Shul and H. J. Kim, *Chem. Mater.*, 2002, **14**, 3823; b) J. H. Yang, H. S. Lee, S. M. Paek and Y. S. Han, *Chem. Lett.*, 2011, **40**, 1242; (c) Y. S. Han, S. Yamanaka and J. H. Choy, *J. Solid State Chem.*, 1999, **144**, 45.
13 (a) C. Ooka, H. Yoshida, K. Suzuki and T. Hattori, *Micropor. Mesopor. Mat.*, 2004, **67**, 143; (b) C. Ooka, S. Akita, Y. Ohashi, T. Horiuchi, K. Suzuki, S. Komai, H. Yoshidac and T. Hattori, *J. Mater. Chem.*, 1999, **9**, 2943; (c) X. Ding, T. An, G. Li, S. Zhang, J. Chen, J. Yuan, H. Zhao, H. Chen, G. Sheng and J. Fu, *J. Colloid Interf. Sci.*, 2008, **320**, 501; (d) D. Chen, G. Du, Q. Ahu and F. Zhou, *J. Colloid Interf. Sci.*, 2013, **409**, 151.
14 J. Pires and M.L. Pinto, etc. in *Pillared Clays and Related Catalysts*, (Eds.: A. Gil, S. A. Korili, R. Trujillano and M. A. Vicente), Springer Science & Business Media, New York, 2010, pp. 23-301.
15 (a) W. J. Ong, L. L. Tan, S. P. Chai, S. T. Yong and A. R. Mohamed, *ChemSusChem*, 2014, **7**, 690; (b) M. R. Hoffmann, S. T. Martin, W. Choi and D. W. Bahnemann, *Chem.Rev.*, 1995, **95**, 69.
16 (a) M. J. Wilson, *A Handbook of Determinative Methods in Clay Mineralogy*, Chapman and Hall, New York, 1987, pp. 60; (b) H. Tateyama, H. Noma, S. Nishimura, Y. Adachi, M. Ooi and K. Urabe, *Clays Clay Miner.*, 1998, **46**, 245.
17 (a) M. Anpo, N. Aikawa, Y. Kubokawa, M. Che, C. Louis and E. Giamello, *J. Phys. Chem.*, 1985, **89**, 5017-5021; (b) J. H. Choy, J. H. Park, J. B. Yoon, *J. Phys. Chem. B*, 1998, **31**, 5991.
18 F. Rouquerol, J. Rouquerol and K. Sing, *Adsorption by Powders and Porous Solids*, Academic press, New York, 1999.
19 T. Allen, *Particle size measurement 4th ed.,* Chapman & Hall, London, New York, 1997, pp. 540-652.
20 (a) G. Horvath and K. Kawazoe, *J. Chem. Eng. Jpn.*, 1983, **16**, 470; (b) R. J. Dombrowski, C. M. Lastoskie and D. R. Hyduke, *Colloid. Surface. A*, 2011, **187–188**, 23.
21 X-ray absorption spectroscopic (XAS) experiments at the Ti K-edge were performed with the X-ray absorption fine structure (XAFS) facility installed at beam line 10C in Pohang Accelerator Laboratory (PAL), Republic of Korea.
22 F. Farges, G. E. Jr. Brown and J. J. Rehr, *Phys. Rev. B*, 1997, **56**, 1809.
23 V. Luca, *J. Phys. Chem. C*, 2009, **113**, 6367.
24 a) M. J. Paek, H. W. Ha, T. W. Kim, S. J. Moon, J. O. Baek, J. H. Choy and S. J. Hwang, *J. Phys. Chem. C*, 2008, **112**, 15966; b) T. W. Kim, M. W. Ha, M. J. Paek, S. H. Hyun, I. H. Baek, J. H. Choy and S. J. Hwang, *J. Phys. Chem. C*, 2008, **112**, 14853; c) S. M. Paek, H. Jung, Y. J. Lee, M. Park, S. J. Hwang and J. H. Choy, *Chem. Mater.*, 2006, **18**, 1134.
25 (a) Y. Lin, C. Ferronato, N. Deng, F. Wu and J. M. Chovelon, *Appl. Catal. B*, 2009, **88**, 32.

